Magnetite−Polypyrrole Metacomposites: Dielectric Properties and Magnetoresistance Behavior

Jiang Guo,[†,¶] Hongbo Gu,[†,¶] Huige Wei,[†,#] Qianyi Zhang,[‡] Neel Haldolaarachchige,[ζ] Ying Li,[‡] David P. Young,[ζ] Suying Wei,*[#] and Zhanhu Guo*[†]

[†]Integrated Composites Lab (ICL), Dan F. Smith Department of Chemical Engineering, Lamar University, Beaumont, Texas 77710, United States

[#]Department of Chemistry and Biochemistry, Lamar University, Beaumont, Texas 77710, United States

[‡]Mechanical Engineering Department, University of Wisconsin−Milwaukee, Milwaukee, Wisconsin 53211, United States

[ζ]Department of Physics and Astronomy, Louisiana State University, Baton Rouge, Louisiana 70803, United States

S *Supporting Information*
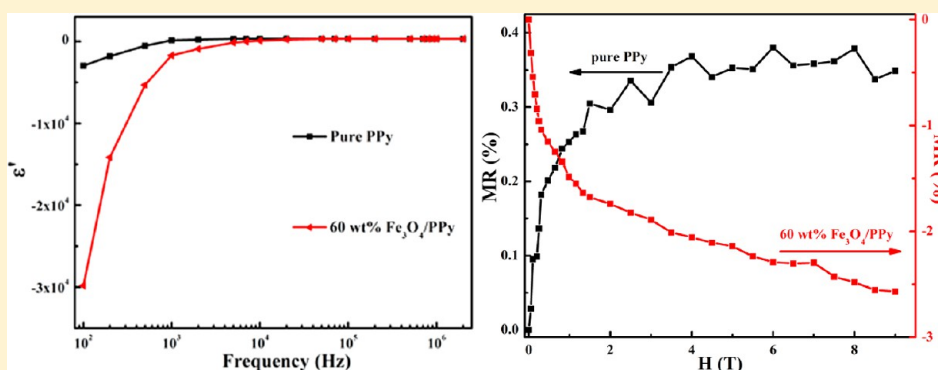
ABSTRACT: The conductive polypyrrole (PPy) polymer nanocomposites (PNCs) reinforced with different magnetite (Fe_3O_4) nanoparticle loadings have been successfully synthesized by using a facile surface initiated polymerization (SIP) method. The scanning electron microscope (SEM) is used to characterize the surface morphology of the as-received Fe_3O_4 nanoparticles (NPs), pure PPy and Fe_3O_4/PPy PNCs. The high-resolution transmission electron microscope (HRTEM) is used to observe the nanoparticle dispersion within the polymer matrix. The chemical structure of the PNCs is characterized by Fourier transform infrared (FT-IR) spectroscopy. The thermal stability of the Fe_3O_4/PPy PNCs is assessed by thermogravimetric analysis (TGA). X-ray diffraction (XRD) results reveal that the addition of NPs has a significant effect on the crystallization of PPy. The switching frequency, at which the permittivity switches from negative to positive, is observed in the synthesized pure PPy and Fe_3O_4/PPy PNCs. The optical band gap of Fe_3O_4/PPy PNCs is studied by ultraviolet−visible diffuse reflectance spectroscopy (UV−vis DRS). The Fe_3O_4/PPy PNCs exhibit no hysteresis loop, indicating the superparamagnetic behavior. Temperature-dependent resistivity indicates a quasi-3-dimensional variable range hopping (VRH) electrical conduction mechanism for the synthesized samples. The positive magnetoresistance (MR) is observed in the synthesized pure PPy at room temperature and analyzed by the wave function shrinkage model. Meanwhile, the negative MR is obtained in the synthesized magnetic PNCs at room temperature and analyzed by the orbital magnetoconductivity theory (forward interference model).

1. INTRODUCTION

Polymer nanocomposites (PNCs) are prepared by dispersing different functional nanoparticles (NPs) into a polymer matrix. Owing to their cost-effective processability, lightweight, flexible, increased tensile strength, larger toughness, tunable mechanical, magnetic and electrical properties[1−3] arising from the combined characteristics of parent constituents into a single material, PNCs have attracted great interest. Conductive PNCs have been extensively investigated because of their potential applications in light emitting devices, batteries, electromagnetic interface shielding,[1] telecoms, electronics, fire retardants, biosensors, electrodes for electrodeposition, and corrosion

resistant coatings.[4] Compared with other conductive polymers including polyaniline (PANI), polythiophene, and poly-(DNTD), polypyrrole (PPy) has attained more attention due to its high electrical conductivity, low cost, easy preparation, high yield, high pseudocapacitance, and environmental stability.[5] PPy has been widely used in gas sensors, biosensors, electromagnetic irradiation shielding materials, electrode

materials, photovoltaic cells, coating materials, and corrosion inhibitors.[2,6,7]

Fe_3O_4 is a mixed iron oxide with a cubic inverse spinel structure, AB_2O_4.[8] In the AB_2O_4, the A site is occupied by Fe^{3+} and the B sites have an equal mix of Fe^{3+} and Fe^{2+}.[9] Fe_3O_4 is a half-metallic ferromagnetic material, in which the density state at the Fermi level $N(E_F)$ is completely polarized and the conductivity is determined by the metallic electron spin charge carriers because of the coexistence of metallic electron spin and insulating electron spin.[10] Because of the unique properties, such as catalytic, magnetic, and electrical properties,[2,11] Fe_3O_4 has been widely applied in many fields such as catalysis, biomedicine, information storage, color imaging, cell separation, and environment remediation.[12,13] Incorporating the Fe_3O_4 NPs into polymer matrix can widen their deployments in electronic, biomedical, and optical fields.[7,14]

Recently, there have been many works on the study of magnetic PPy PNCs. For example, Dey et al.[15] have prepared the Fe_3O_4/PPy PNCs with a very large dielectric constant using ammonium peroxodisulfate (APS) as oxidant. Chen et al.[16] have synthesized Fe_3O_4/PPy using the common ion effect and studied the influence of concentration of oxidant $FeCl_3$ solution on the properties of PPy/Fe_3O_4 composites, which show the electrical and ferromagnetic properties. Wang et al.[17] have successfully encapsulated Fe_3O_4 with PPy via emulsion polymerization using polyvinyl alcohol as a surfactant and studied the application of Fe_3O_4/PPy in biomedicine application. Chen et al.[18] have prepared the Fe_3O_4/PPy PNCs and investigated magnetic and electrical properties of Fe_3O_4/PPy PNCs. However, the negative permittivity and magnetoresistance (MR) of Fe_3O_4/PPy PNCs have been rarely reported so far.

Metamaterials formed from either periodic or random arrays of scattering elements are artificial materials.[19,20] The two macroscopic electromagnetic parameters (the electric permittivity ε, and the magnetic permeability μ) are used to characterize the metamaterials.[20] Compared with conventional materials, metamaterials can exhibit unique electromagnetic behaviors due to the negative permittivity and negative permeability at a certain frequency.[21] The metamaterials can be used to design invisibility devices (such as invisibility cup),[22] super lenses,[21] and cloaking.[23]

MR is a phenomenon that reflects the resistance change of a material under an external magnetic field.[24] The MR effect observed in the organic materials is called organic magnetorsistance (OMAR),[25] which is related to the formation of the excitons and caused by the trapping of charge carrier at triplet excitons.[26] There are many studies on the MR effect of PPy polymer reinforced with different nanoparticles. For example, Abou-Elazab et al.[27] have found the positive MR in the PPy, which is prepared by electrochemical oxidation of pyrrole and doped with tetraethylammonium toluene-4-sulfonate. Long et al.[28] have studied the negative MR of multiwalled carbon nanotube/PPy synthesized using an in situ chemical oxidative polymerization method. However, there are no reports regarding the negative MR of the Fe_3O_4/PPy PNCs.

In this work, Fe_3O_4/PPy PNCs are synthesized by using the surface initiated polymerization (SIP) method. The Fourier transform infrared (FT-IR) spectroscopy is used to characterize the chemical structure of the as-received Fe_3O_4 NPs, pure PPy, and Fe_3O_4/PPy PNCs. The thermal stability of the Fe_3O_4/PPy PNCs is performed by thermogravimetric analysis (TGA). The effects of Fe_3O_4 NPs on the crystallization of the PPy are also studied by X-ray diffraction (XRD). Scanning electron microscope (SEM) and a high-resolution transmission electron microscope (HRTEM) are used to depict the dispersion and morphology of the as-received Fe_3O_4 NPs, pure PPy, and Fe_3O_4/PPy PNCs. The frequency-dependent permittivity, temperature-dependent resistivity, MR, optical properties, and magnetic properties are systematically investigated as well. The positive magnetoresistance (MR) observed in the synthesized pure PPy at room temperature is analyzed by the wave function shrinkage model and the negative MR obtained in the synthesized magnetic PNCs at room temperature is analyzed by the orbital magnetoconductivity theory (forward interference model), respectively.

2. EXPERIMENTAL SECTION

2.1. Materials. Pyrrole (C_4H_5N, ≥98%), ammonium persulfate (APS, $(NH_4)_2S_2O_8$, 98%), and p-toluene sulfonic acid (PTSA, $C_7H_8O_3S$, ≥98.5%) were purchased from Sigma-Aldrich. The Fe_3O_4 NPs were obtained from Nanjing Emperor Nano Material Co., Ltd., China. All the chemicals were used as-received without any further treatment.

2.2. Fabrication of Fe_3O_4/PPy PNCs. Fe_3O_4/PPy PNCs were fabricated by using the SIP method. First, the Fe_3O_4 NPs were dispersed in an aqueous solution containing PTSA (15 mmol) and APS (9 mmol) in 100 mL of deionized water by 1-h sonication (Branson 8510) and mechanical stirring (SCILO-GEX OS20-Pro LCD Digital Overhead Stirrer, 300 rpm) in an ice−water bath. Second, the pyrrole solution (18 mmol, 25 mL deionized water) was mixed with the above Fe_3O_4 NPs suspension and mechanically and ultrasonically stirred continuously for an additional 1.5 h in the ice−water bath for further polymerization. The product was vacuum filtered and washed with deionized water several times. The precipitant was further washed with 1 mol L^{-1} PTSA. The final synthesized nanocomposites were dried at 60 °C in an oven overnight. The Fe_3O_4/PPy PNCs with a nanoparticle loading of 10, 20, 40, and 60 wt % were fabricated, respectively. The pure PPy was fabricated following the above procedures without adding any NPs for comparison.

2.3. Characterizations. The Fourier transform infrared (FT-IR) spectra of the products were obtained on a Bruker Inc. Vector 22 (coupled with an ATR accessory) in the range of 500 to 2200 cm^{-1} at a resolution of 4 cm^{-1}. TGA analysis was conducted by TA Instruments TGA Q-500 with a heating rate of 10 °C min^{-1} under an air-flow rate of 60 mL min^{-1} from 25 to 700 °C. XRD was measured by D/max-rB wide-angle X-ray diffractometer at a Cu Kα wavelength of 0.154 nm. The scanning rate is 4° min^{-1} from 10 to 80°. The SEM was performed in a JEOL JSM-6510LV system after coating with carbon. The HRTEM was performed on the Hitachi H9000NAR. Dielectric properties were investigated by a LCR meter (Agilent, E4980A) equipped with a dielectric test fixture (Agilent, 16451B) at the frequency of 20 to 2×10^6 Hz at room temperature. Pure PPy and Fe_3O_4/PPy PNCs were pressed in a form of disc pellet with a diameter of 25 mm by applying a pressure of 50 MPa in a hydraulic presser and the average thickness of the samples was about 0.6 mm. The same samples were also used to measure the resistivity, MR, and ultraviolet−visible diffuse reflectance spectroscopy (UV−vis DRS). The resistivity was measured by a standard four-probe method from 100 to 290 K. The temperature-dependent resistivity was used to determine the electrical conduction mechanism in the pure PPy and Fe_3O_4/PPy PNCs. UV−vis DRS of pure PPy and
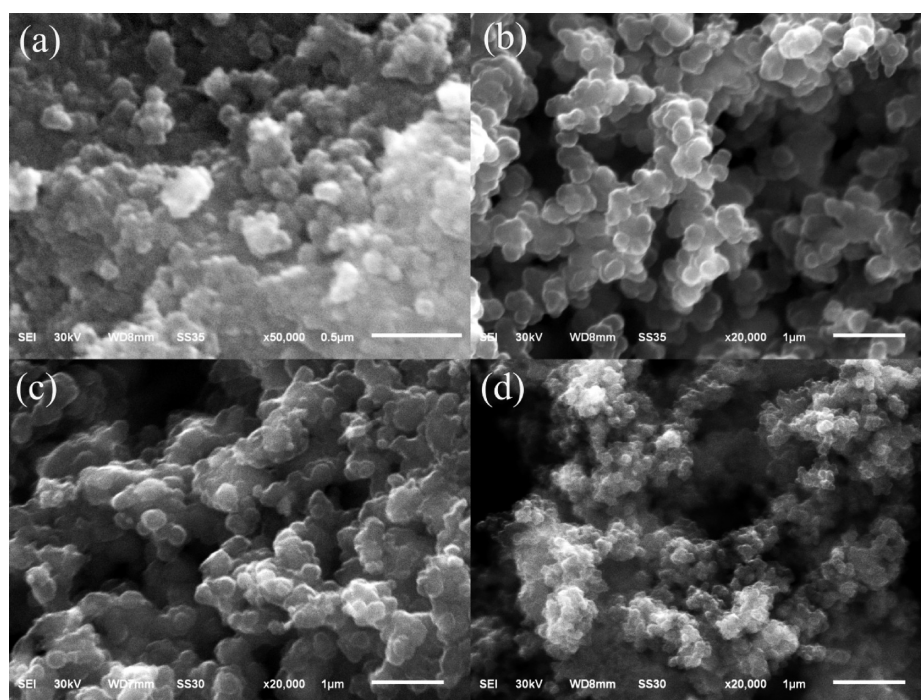
Figure 1. SEM micrographs of (a) as-received Fe_3O_4 NPs, (b) pure PPy, and Fe_3O_4/PPy PNCs with a Fe_3O_4 nanoparticle loading of (c) 20 and (d) 60 wt %, respectively.
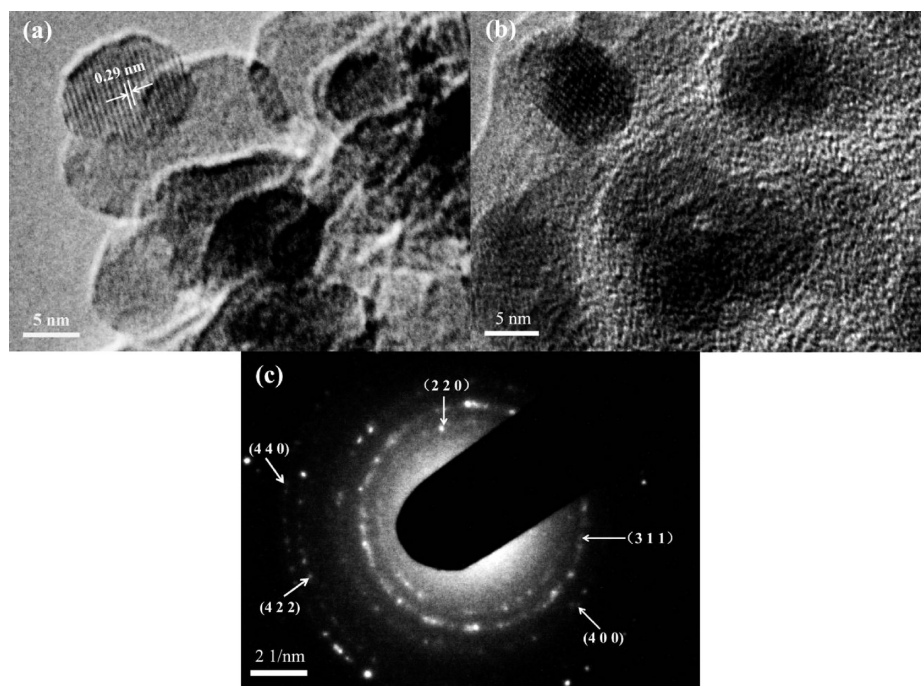

Figure 2. HRTEM images of (a) as-received Fe_3O_4 NPs, (b) Fe_3O_4/PPy PNCs with a Fe_3O_4 nanoparticle loading of 40 wt %, and (c) selected area electron diffraction (SAED) of Fe_3O_4/PPy PNCs with a Fe_3O_4 nanoparticle loading of 40 wt %.

Fe_3O_4/PPy PNCs was recorded on a UV/vis/NIR spectropho-tometer (PC, JASCO Model V-670) equipped with a Jasco ISN-723 diffuse reflectance accessory. MR was carried out with use of a standard four-probe technique by a 9-T Physical Properties Measurement System (PPMS) by Quantum Design at room temperature. The magnetic properties were also investigated in a 9-T Physical Properties Measurement System (PPMS) by Quantum Design.

3. RESULTS AND DISCUSSION

3.1. SEM and HRTEM Observations. Figure 1 shows the SEM images of the as-received Fe_3O_4 NPs, pure PPy, and Fe_3O_4/PPy PNCs with a Fe_3O_4 nanoparticle loading of 20 and 60 wt %. The as-received Fe_3O_4 NPs, Figure 1a, are ball-like with an average diameter of 59.61 nm measured by Nano measure software. The pure PPy, Figure 1b, shows particulate structure with a fairly uniform size distribution and is observed

to be relatively loosely packed compared to the Fe_3O_4/PPy PNCs, Figure 1c,d. The surface of the as-received Fe_3O_4 NPs is smooth. However, the surface of the Fe_3O_4/PPy PNCs becomes rougher due to the polymerization that occurred on the surface of Fe_3O_4 NPs. The HRTEM images of the as-received Fe_3O_4 NPs and the Fe_3O_4/PPy PNCs with a Fe_3O_4 nanoparticle loading of 40 wt % are shown in Figure 2a,b. The HRTEM image of the as-received Fe_3O_4 NPs, Figure 2a, shows that the average diameter of Fe_3O_4 NPs is about 11.14 nm measured by Nano measure software. However, this result is different from that observed in the SEM (59.61 nm), Figure 1a, in which some of the Fe_3O_4 NPs agglomerate together because of the magnetic dipole−dipole interactions (also called dipolar coupling, which means direct interaction between two magnetic dipoles) between Fe_3O_4 NPs.[29] The clear lattice fringes presented in Figure 2a indicate the highly crystallized as-received Fe_3O_4 NPs. The lattice fringe *d*-spacing value (interplanar distance) of the as-received Fe_3O_4 NPs is about 0.29 nm, which corresponds to the (2 2 0) crystallographic plane (which examines the arrangement of atoms in solids) of Fe_3O_4.[30] Figure 2b shows the microstructure of the Fe_3O_4/PPy PNCs with a Fe_3O_4 nanoparticle loading of 40 wt %, which consists of the crystalline Fe_3O_4 inside and the amorphous PPy polymer layer outside. The crystal structure of the Fe_3O_4/PPy PNCs with a Fe_3O_4 loading of 40 wt % is identified by the selected area electron diffraction (SAED), Figure 2c. The calculated *d*-spacing values of 2.94, 2.56, 2.08, 1.61, and 1.49 Å correspond to the (2 2 0), (3 1 1), (4 0 0), (4 2 2), and (4 4 0) crystallographic planes of Fe_3O_4.[31] Figure S1 shows the acid dissolubility of the as-received Fe_3O_4 NPs and the synthesized Fe_3O_4/PPy PNCs with a Fe_3O_4 loading of 60 wt %. The Fe_3O_4 NPs are observed to dissolve in the 1.0 mol L^{-1} hydrochloric acid (HCl) solution and the color changes to yellow. However, the Fe_3O_4/PPy PNCs are observed not to dissolve in the same acid solution, which indicates that Fe_3O_4 NPs have been successfully protected by the PPy matrix.

3.2. FT-IR Analysis. Figure 3 shows the FT-IR spectra of the as-received Fe_3O_4 NPs, pure PPy, and Fe_3O_4/PPy PNCs with different Fe_3O_4 nanoparticle loadings. For the as-received Fe_3O_4 NPs, Figure 3a, the peak around 529 cm^{-1} is due to the vibration of the Fe—O band.[8] For the pure PPy, Figure 3b, the peaks located at 1521 and 1431 cm^{-1} are due to the C=C and

C—N stretching vibration, respectively.[2,6,7] The C—C vibration is reflected at a peak of 1132 cm^{-1}.[32] The peaks at 1276 and 1007 cm^{-1} are assigned to the C—H in-plane and out-of-plane deformation vibration, respectively.[32] The small band located at 960 cm^{-1} is assigned to the C—C out-of-plane deformation vibration.[32] These characteristic peaks (1521, 1431, 1276, 1132, 1007, and 960 cm^{-1}) of the pure PPy are also observed in the Fe_3O_4/PPy PNCs, Figure 3c−f. However, these characteristic peaks have some shifts (about 7−16 cm^{-1}) compared with those of the pure PPy, indicating the interaction between the Fe_3O_4 NPs and the polymer matrix.[8] These results indicate that the Fe_3O_4/PPy PNCs have been successfully synthesized.

3.3. Thermogravimetric Analysis. Figure 4 shows the TGA curves of the as-received Fe_3O_4 NPs, pure PPy, and
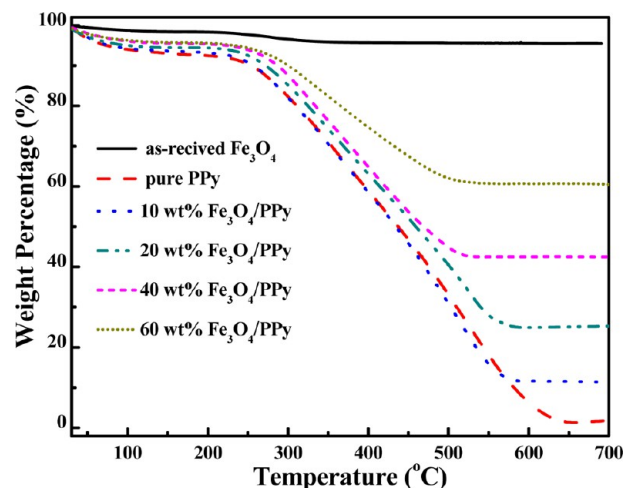
Figure 4. TGA curves of as-received Fe_3O_4 NPs, pure PPy, and Fe_3O_4/PPy PNCs with a Fe_3O_4 nanoparticle loading of 10, 20, 40, and 60 wt %.

Fe_3O_4/PPy PNCs with a Fe_3O_4 nanoparticle loading of 10, 20, 40, and 60 wt %. For the as-received Fe_3O_4 NPs, the weight has only a slight change within the measured temperature range from 35 to 700 °C.[13] Two weight loss regions are observed in the TGA curves of pure PPy and its Fe_3O_4 PNCs. The steady weight loss from 30 to 240 °C is due to the elimination of the moisture and dopant anions in the samples.[8] The major weight loss of all the synthesized samples from 240 to 650 °C is due to the decomposition of PPy.[1] The 10% weight loss decomposition temperature for the pure PPy and Fe_3O_4/PPy PNCs with a Fe_3O_4 nanoparticle loading of 10, 20, 40, and 60 wt % are 254, 257, 272, 287, and 300 °C, respectively. This result indicates that the thermal stability of the Fe_3O_4/PPy PNCs is improved by the addition of Fe_3O_4 NPs and increases with increasing Fe_3O_4 nanoparticle loading, which is also observed in the γ-Fe_2O_3/PPy PNCs system.[7] Interestingly, it is found that the TGA curves of Fe_3O_4/PPy PNCs reach a plateau at a certain temperature. The temperature to reach the plateau decreases with increasing nanoparticle loading. The higher the nanoparticle loading, the lower the PPy weight percentage obtained, thus the PNCs with high nanoparticle loadings would reach the plateau at low temperature. At high temperature, the Fe_3O_4 NPs get oxidized to form hematite (α-Fe_2O_3).[33] The weight residue of pure PPy at 700 °C is about 1.83 wt % arising from the carbonized PPy, which indicates that PPy cannot easily become completely decomposed in the air even at a

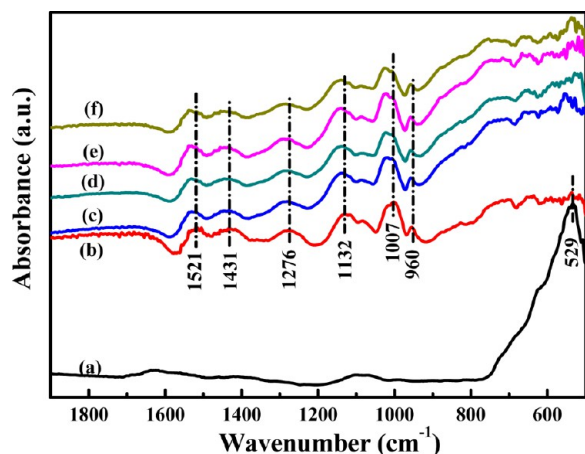**Figure 3.** FT-IR spectra of (a) Fe_3O_4 NPs, (b) pure PPy, and Fe_3O_4/PPy PNCs with a Fe_3O_4 nanoparticle loading of (c) 10, (d) 20, (e) 40, and (f) 60 wt %, respectively.

higher temperature.[2] The weight residue for the α-Fe$_2$O$_3$ is calculated to be 11.39, 25.28, 42.42, and 60.47 wt % for the Fe$_3$O$_4$/PPy PNCs with a Fe$_3$O$_4$ loading of 10, 20, 40, and 60 wt %, respectively. The weight percentage of Fe$_3$O$_4$ is calculated to be 11.01, 24.44, 41.01, and 58.45 wt %, respectively.

3.4. X-ray Diffraction Analysis. Figure 5 shows the XRD patterns of the as-received Fe$_3$O$_4$ NPs, pure PPy, and Fe$_3$O$_4$/
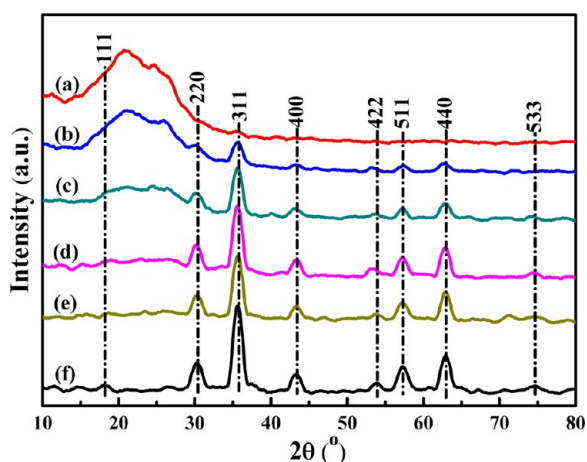

Figure 5. The XRD patterns of (a) pure PPy, and the Fe$_3$O$_4$/PPy PNCs with a nanoparticle loadings of (b) 10, (c) 20, (d) 40, and (e) 60 wt %, respectively, and (f) as-received Fe$_3$O$_4$ NPs.

PPy PNCs with different Fe$_3$O$_4$ nanoparticle loadings. Only a broad diffraction peak located at 2θ = 15.2–27.9° is observed in the pure PPy,[31] Figure 5a, indicating the amorphous behavior of the pure PPy. The diffraction peaks at 2θ = 18.0, 30.3, 35.6, 43.3, 54.0, 57.2, 62.9, and 74.6° in the XRD curve of Fe$_3$O$_4$ NPs, Figure 5f, correspond to (1 1 1), (2 2 0), (3 1 1), (4 0 0), (4 2 2), (5 1 1), (4 4 0), and (5 3 3) crystallographic planes of the spinel phase of Fe$_3$O$_4$, respectively.[31] The XRD patterns of the crystallite structure can be used to estimate the lattice plane d-spacing and average crystallite size.[34] Generally, the lattice plane d-spacing is calculated based on the Bragg formula, eq 1:[34]

$$\lambda = 2d \sin \theta \tag{1}$$

where λ is the X-ray wavelength (λ = 0.154 nm) and θ is the diffraction angle. The average crystallite size can be estimated by the XRD pattern, using the Scherrer formula,[8] eq 2:

$$L = \frac{k\lambda}{\beta \cos \theta} \tag{2}$$

where λ = 0.154 nm, L is the average crystallite size, β is the full-width at half-maximum, and θ is the diffraction angle; the shape factor k, depending on the miller index of the reflection plane and the shape of the crystal, is normally 0.89. The peak of the as-received Fe$_3$O$_4$ NPs at 2θ = 35.6° is chosen to calculate the lattice plane d-spacing and average crystallite size. The obtained lattice plane d-spacing and average crystallite size of the as-received Fe$_3$O$_4$ NPs are about 0.25 (which corresponds to the (3 1 1) crystallographic plane of Fe$_3$O$_4$) and 10.28 nm, respectively. The obtained average crystallite size (10.28 nm) of as-received Fe$_3$O$_4$ NPs is consistent with the results obtained in HRTEM (11.14 nm). The peaks of the Fe$_3$O$_4$/PPy PNCs with a Fe$_3$O$_4$ nanoparticle loading of 60 wt % at 2θ = 35.6° are also chosen to calculate the lattice plane d-spacing and the average crystallite size. The calculated lattice plane d-spacing and

average crystallite size of the Fe$_3$O$_4$/PPy PNCs with a Fe$_3$O$_4$ loading of 60 wt % are about 0.25 and 11.5 nm, respectively. Obviously, the Fe$_3$O$_4$/PPy PNCs have the diffraction peaks of the Fe$_3$O$_4$ NPs, Figure 5b–e, and the intensity of the peaks becomes stronger with increasing the Fe$_3$O$_4$ nanoparticle loading. However, the broad peak of pure PPy at 2θ = 15.2–27.9° shows a reduced intensity with increasing the Fe$_3$O$_4$ nanoparticle loading, indicating a strong effect of the Fe$_3$O$_4$ NPs on the crystallization of PPy. This is also observed in the Fe$_3$O$_4$/PANI PNCs.[8]

3.5. Dielectric Properties. Figure 6 shows the real permittivity (ε'), imaginary permittivity (ε''), and dielectric loss tangent (tan δ, where tan δ = $\varepsilon''/\varepsilon'$) as a function of frequency at room temperature for pure PPy and its Fe$_3$O$_4$ PNCs with a Fe$_3$O$_4$ nanoparticle loading of 10, 20, 40, and 60 wt %, respectively. In Figure 6a, the ε' for pure PPy and its Fe$_3$O$_4$ PNCs switches from negative to positive and increases with increasing the frequency from 10^2 to 10^4 Hz. This frequency-dependent property is contributed to the interfacial polarization,[1] where the charge carriers are accumulated at the internal interfaces arising from the Maxwell–Wagner–Sillars polarization effect (which occurs on a mesoscopic scale either at the inner dielectric boundary layers or at the external electrode–sample interface).[35] The inset of Figure 6a shows the positive ε' value within the frequency range from 10^4 to 2×10^6 Hz. The decrease of ε' at high frequency is induced by the well-known dielectric relaxation phenomena,[23] which is usually caused by the delay of molecular polarization in an external alternative electric field.[36] The Fe$_3$O$_4$/PPy PNCs with a Fe$_3$O$_4$ nanoparticle loading of 60 wt % have the highest value of ε' compared with the Fe$_3$O$_4$/PPy PNCs with other loadings of Fe$_3$O$_4$ at high frequency (>2 × 10^4 Hz), Figure 6a. Figure 6b shows the ε'' of pure PPy and its Fe$_3$O$_4$ PNCs with a Fe$_3$O$_4$ nanoparticle loading of 10, 20, 40, and 60 wt %, respectively. The ε'' of pure PPy shows the large negative values (about the order of -10^7) and increases with increasing frequency at low frequency (<10^3 Hz), then decreases monotonically after 10^3 Hz. For the Fe$_3$O$_4$/PPy PNCs, the ε'' also shows a switch from negative to positive at certain frequency. The ε'' of the Fe$_3$O$_4$/PPy PNCs with a Fe$_3$O$_4$ nanoparticle loading of 10 and 20 wt % exhibits a similar trend as that of pure PPy. The ε'' value of the 40 wt % Fe$_3$O$_4$/PPy PNCs increases with increasing frequency from 10^2 to 2×10^3 Hz, and then decreases with increasing frequency (>2 × 10^3 Hz). The ε'' of the Fe$_3$O$_4$/PPy PNCs with a Fe$_3$O$_4$ nanoparticle loading of 60 wt % also shows large negative values (about the order of -10^7) and increases with increasing frequency from 10^2 to 10^4 Hz, and then decreases with increasing frequency (>10^4 Hz). Generally, according to the Drude–Lorentz model, the dielectric permittivity of the conductive materials can be expressed as eq 3[37]

$$\varepsilon(\omega) = 1 - \frac{\omega_p^2}{\omega(\omega + i\gamma)} \tag{3}$$

where ω_p is the plasma frequency, γ is the damping constant, and ω is the angular frequency. When $\omega < \omega_p$, the real permittivity ε' is negative; while $\omega > \omega_p$, the ε' is positive.

Figure 6c shows the frequency-dependent tan δ for pure PPy and its Fe$_3$O$_4$ PNCs with a Fe$_3$O$_4$ nanoparticle loading of 10, 20, 40, and 60 wt %, respectively. The tan δ for all the samples increases from the frequency of 10^2 Hz and then reaches a peak value at different frequencies depending on the filler loading,
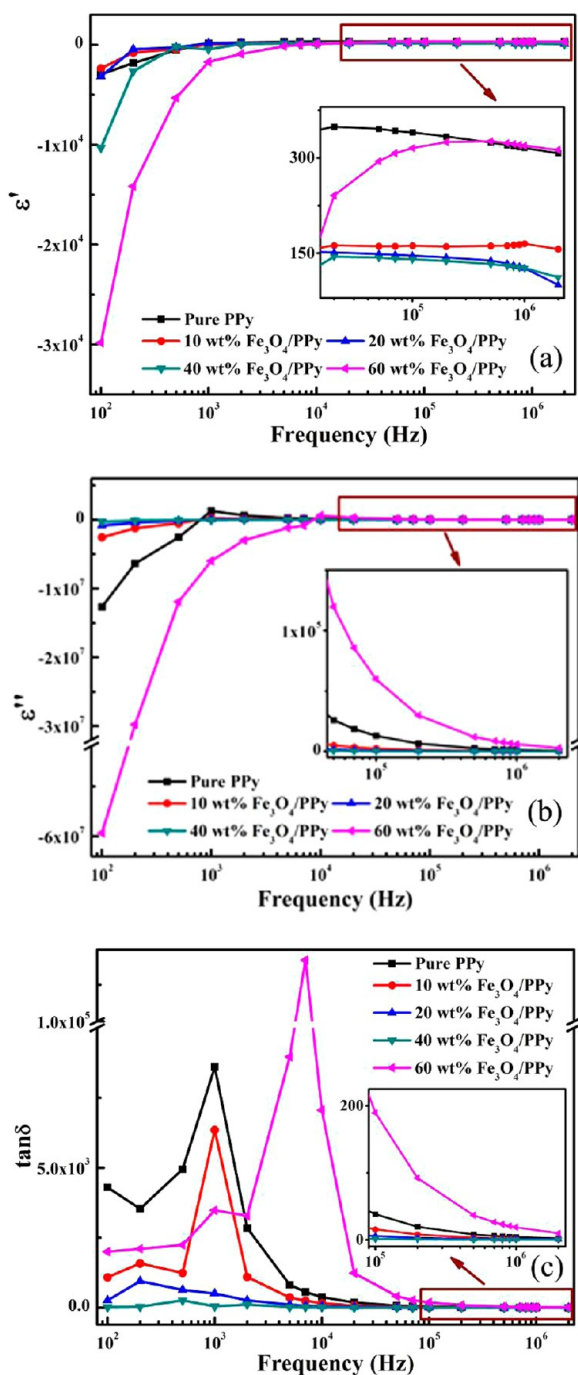
Figure 6. Dependence of dielectric permittivity of pure PPy and Fe$_3$O$_4$/PPy PNCs on frequency: (a) ε' from 10^2 to 2×10^6 Hz; (b) ε'' from 10^2 to 2×10^6 Hz; and (c) tan δ from 10^2 to 2×10^6 Hz.

after that the tan δ decreases with increasing frequency. The appearance of the peak in the tan δ is due to the resonance effect, in which the system tends to oscillate with greater amplitude than others at certain frequencies, especially for the negative permittivity values.[38] The tan δ is very low at high frequency (>10^5 Hz) for all the samples. The materials with a very low energy loss have a potential to be applied in the microelectronic devices.[39]

3.6. Optical Properties. Bad gap, which is also called energy gap, $E_{(t)}$, is the energy range between the conduction band and the valence band.[40,41] The conduction band is the electron energy range for the electron to move freely within the

atomic lattice of the materials, which is the first unfilled energy level at absolute zero temperature (called lowest unoccupied molecular orbital, LUMO, for molecules). The valence band is the highest energy range and the last filled energy level (highest occupied molecular orbital, HOMO, for molecules).[42] In the inorganic materials, as the exciton binding energy $E_t - E_g^{opt}$ (the difference between E_t and E_g^{opt}, E_g^{opt} is the optical band gap) is very small, the E_t is very close to E_g^{opt}. In the organic materials, the exciton binding energy is larger than that in the inorganic materials, therefore, E_t is larger than E_g^{opt}. The exciton binding energy can be measured by inverse photoelectron spectroscopy (IPES) and ultraviolet photoelectron spectroscopy (UPS).[43] In this work, the UV−vis DRS is used to measure the UV−vis absorption edge (λ_{edge}) of all the samples. λ_{edge} means the transition between the strong short-wavelength and the weak long-wavelength absorption in the spectrum of a solid sample.[44] The optical band gap energy can be obtained according to eq 4, which is based on the onset of UV−vis DRS of the powdered materials:[45,46]

$$E_g^{opt}(eV) = 1240/\lambda_{edge}(nm) \tag{4}$$

where E_g^{opt} is the optical band gap that can be used to analyze the optical absorption and the number 1240 is obtained from the relationship between frequency and wavelength as described by eq 5:

$$E(eV) = h\upsilon = h\frac{c}{e\lambda} \tag{5}$$

where h is Planck's constant, c is about 3×10^8 m s^{-1}, the speed of light in the vacuum, e is the electron charge, the unit of λ is meter (m), then 1240 can be obtained from hc/e.

It is reported that the dopant has a significant effect on the band gap of PPy. The band gap of the undoped PPy differs from that of the doped PPy[47] and different dopants can make the band gap of PPy different.[48] Figure 7 shows the UV−vis
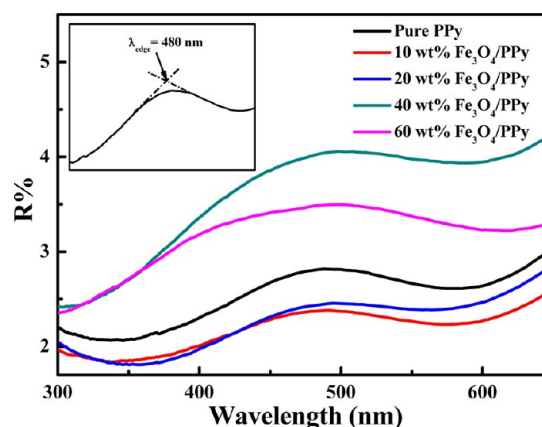

Figure 7. UV−vis DRS of pure PPy and Fe$_3$O$_4$/PPy PNCs with a Fe$_3$O$_4$ nanoparticle loading of 10, 20, 40, and 60 wt %.

DRS of pure PPy and its Fe$_3$O$_4$ PNCs with a Fe$_3$O$_4$ nanoparticle loading of 10, 20, 40, and 60 wt %, respectively. The λ_{edge} is related to the $\pi-\pi^*$ transition in the polymer chain of PPy.[49] The λ_{edge} of pure PPy calculated by the onset of the UV−vis DRS in Figure 7 is 480 nm and the E_g^{opt} of pure PPy is 2.58 eV, which is estimated according to eq 4. The calculated E_g^{opt} of pure PPy is consistent with the results investigated previously in the HCl acid doped PPy (2.54 eV)[48] and in the iodine doped PPy (2.86 eV).[47] The λ_{edge} and E_g^{opt} of the Fe$_3$O$_4$/

PPy nanocomposites with different nanoparticle loadings are listed in Table 1. From Table 1, it is obtained that the addition of Fe_3O_4 NPs into the PPy matrix is observed to have little effect on the E_g^{opt} of PPy.

Table 1. Absorption Edge and Optical Band Gap of Pure PPy and Fe_3O_4/PPy PNCs with a Fe_3O_4 Nanoparticle Loading of 10, 20, 40, and 60 wt %

samples	absorption edge of PANI (λ_{edge}, nm)	optical band gap of PANI (E_g^{opt}, eV)
pure PPy	480	2.58
10 wt % Fe_3O_4/PPy	476	2.61
20 wt % Fe_3O_4/PPy	490	2.53
40 wt % Fe_3O_4/PPy	474	2.62
60 wt % Fe_3O_4/PPy	468	2.65

3.7. Magnetic Properties. Magnetization is a phenomenon that describes the response of magnetic materials to an applied external magnetic field.[50] Application of a magnetic field can make the direction of magnetic moment of the NPs the same as the field direction, and the magnetization increases with increasing magnetic field until it reaches the saturation magnetization (M_s).[51] When the diameter of the magnetic NPs is around 10 nm, according to the materials, the coercive force (H_c) reaches zero, then the NPs will be in the superparamagnetic state. The magnetic properties of a superparamagnetic system can be described on the basis of the Langevin eq 6:[52]

$$M = \int_0^\infty L\left(\frac{mH}{k_BT}\right)f(m)\,dm \tag{6}$$

where M is magnetization (emu g^{-1}) in H (Oe), k_B is the Boltzmann constant, m is the magnetic moment, T is the absolute temperature, and $f(m)$ is the distribution function of magnetic moments related to the saturation magnetization (M_s) as described by eq 7:

$$M_s = \int_0^\infty f(m)\,dm \tag{7}$$

According to eq 6 and 7, the relationship between M and M_s can be described by eq 8:

$$\frac{M}{M_s} = \coth x - \frac{1}{x} \tag{8}$$

where, $x = aH$; the parameter a is related to the electron spin magnetic moment m of the individual molecule as described in eq 9:

$$a = \frac{m}{k_BT} \tag{9}$$

Figure 8 shows the magnetization curves of the as-received Fe_3O_4 NPs, pure PPy, and Fe_3O_4/PPy PNCs with a Fe_3O_4 nanoparticle loading of 10, 20, 40, and 60 wt % at room temperature, respectively. All the samples show no hysteresis loop, which means that the H_c is zero Oe, indicating a superparamagnetic behavior.[53] The magnetization of all the samples did not reach saturation at the measured magnetic field. Thus, the M_s is determined by the extrapolated M_s
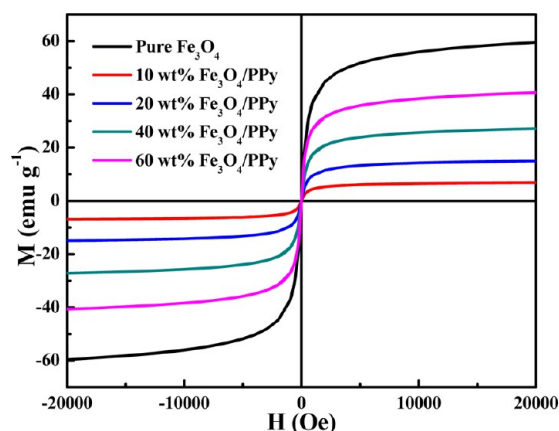

Figure 8. Room temperature magnetization as a function of magnetic field for the as-received Fe_3O_4 NPs, pure PPy, and Fe_3O_4/PPy PNCs with different Fe_3O_4 nanoparticle loadings of 10, 20, 40, and 60 wt %, respectively.

obtained from the intercept of M–H^{-1} at high magnetic field.[54] The M_s of the as-received Fe_3O_4 NPs is 63.45 emu g^{-1}, which is smaller than that of the bulk Fe_3O_4 (92 emu g^{-1}).[55] The obtained M_s values of Fe_3O_4/PPy PNCs with a Fe_3O_4 nanoparticle loading of 10, 20, 40, and 60 wt % are 7.32, 15.7, 28.81, and 43.11 emu g^{-1}, respectively.

The best fit to eq 8 is obtained by nonlinear fitting of M and H, using Polymath software. The a for the as-received Fe_3O_4 NPs and Fe_3O_4/PPy PNCs with a Fe_3O_4 nanoparticle loading of 10, 20, 40, and 60 wt % is 3.24×10^{-3}, 3.20×10^{-3}, 3.28×10^{-3}, 3.22×10^{-3}, and 3.31×10^{-3} T^{-1}, respectively. According to eq 9, the magnetic moment m can be calculated from a. The m of the pure PPy and Fe_3O_4/PPy PNCs with a Fe_3O_4 nanoparticle loading of 10, 20, 40, and 60 wt % is 1.40, 1.38, 1.42, 1.39, and 1.43 μ_B, respectively. The m is almost the same for all the samples, indicating that the polymer has little effect on the magnetic moment of the Fe_3O_4 NPs.

3.8. Temperature-Dependent Resistivity and Electrical Conduction Mechanism. The temperature-dependent resistivity of pure PPy and its Fe_3O_4 PNCs with different Fe_3O_4 nanoparticle loadings is measured at temperatures ranging from 100 to 290 K to determine the electrical conduction mechanism. In Figure 9a, the resistivity of all the synthesized samples decreases with increasing temperature, which is a typical behavior of the semiconductor.[6] The resistivity of pure PPy decreases from 4.60 to 1.58 ohm·cm within the measured temperature scale. The resistivity of the Fe_3O_4/PPy PNCs with different Fe_3O_4 nanoparticle loadings varies from 2.15 to 30.01 ohm·cm within the temperature scale 100−290 K. The Fe_3O_4/PPy PNCs exhibit higher resistivity than that of pure PPy over the whole temperature range and the resistivity of the Fe_3O_4/PPy PNCs increases with increasing the Fe_3O_4 nanoparticle loading.

To better understand the charge transport in pure PPy and its Fe_3O_4 PNCs, the Mott variable range hopping (VRH) model, eq 10, is used to describe the electrical conduction mechanism:[2,7,23]

$$\sigma = \sigma_0 \exp\left[-\left(\frac{T_0}{T}\right)^{1/1+n}\right]; \qquad n = 1, 2, 3 \tag{10}$$

where the pre-exponential factor σ_0 is a constant, which represents the conductivity at infinite low temperature limit.
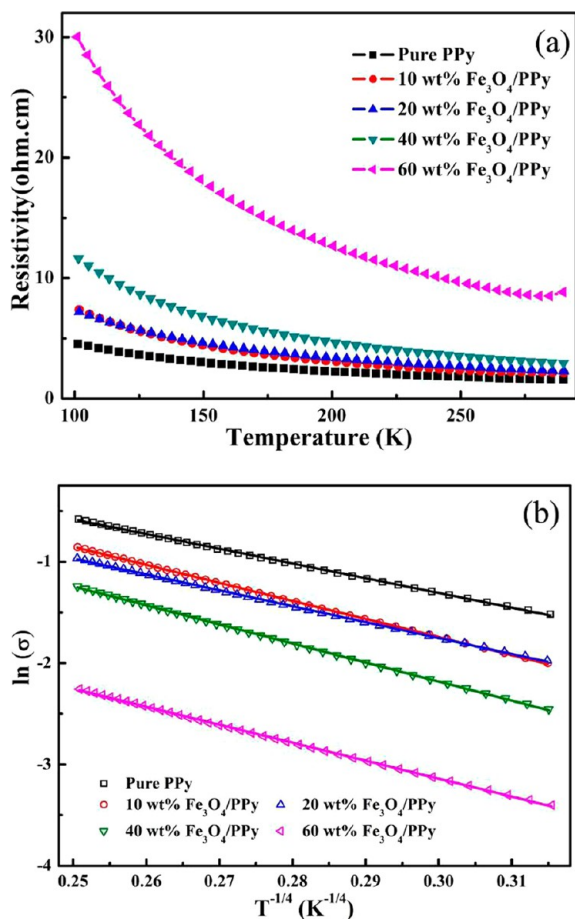
Figure 9. (a) Resistivity vs temperature and (b) ln σ−T^{−1/4} curves of pure PPy and Fe_3O_4/PPy PNCs with a Fe_3O_4 nanoparticle loading of 10, 20, 40, and 60 wt %.

The n value of 3, 2, and 1 is for three-, two-, and one-dimensional systems, respectively.[56] T is the Kelvin temperature (K) and T_0 is the characteristic Mott temperature (K) and is expressed as eq 11:[57]

$$T_0 = 24/[\pi k_B N(E_F) a_0^3] \qquad (11)$$

where k_B is Boltzmann constant, the $N(E_F)$ is the density of states at the Fermi level, and a_0 is the localization length of the localized wave function of charge carriers.[57] Equation 10 can be rearranged to the following eq 12:

$$\ln \sigma = \ln \sigma_0 - \left(\frac{T_0}{T}\right)^{1/1+n}; \qquad n = 1, 2, 3 \qquad (12)$$

Thus, σ_0 and T_0 can be calculated from the intercept and slope of the plot ln σ−T^{−1/(1+n)}, respectively. The obtained results from temperature-dependent resistivity, Figure 9a, are shown in Figure 9b. Both pure PPy and the Fe_3O_4/PPy PNCs are observed to follow the ln σ−T^{−1/4} linear relationship, which indicates a quasi-3-dimentional VRH mechanism. The σ_0 and T_0 obtained from Figure 9b are summarized in Table 2. Generally, a larger T_0 indicates a stronger localization of the charge carriers, which is usually accompanied by an increased resistivity.[58] A smaller T_0 indicates a weak localization.[59] The T_0 of the Fe_3O_4/PPy PNCs is higher than that of pure PPy, which means that the resistivity increases after adding the Fe_3O_4 NPs. Interestingly, it is observed that the optical band gap E_g^{opt} of the

Table 2. T_0, σ_0, and ρ_r for the Pure PPy and Fe_3O_4/PPy PNCs with a Fe_3O_4 Nanoparticle Loading of 10, 20, 40, and 60 wt %

samples	$T_0 \times 10^4$ (K)	σ_0 (S cm^{-1})	ρ_r
pure PPy	4.46 ± 0.06	21.14 ± 0.29	2.89
10 wt % Fe_3O_4/PPy	10.1 ± 0.08	36.65 ± 0.36	3.43
20 wt % Fe_3O_4/PPy	6.07 ± 0.07	19.20 ± 0.23	3.15
40 wt % Fe_3O_4/PPy	12.46 ± 0.11	31.65 ± 0.36	3.95
60 wt % Fe_3O_4/PPy	9.92 ± 0.12	8.88 ± 0.13	3.39

pure PPy and Fe_3O_4/PPy PNCs with a nanoparticle loading of 10, 20, and 40 wt % have the same trend with the T_0, which confirms that the band gap determines both the electrical and optical properties of the semiconducting polymers.[60] As the Fe_3O_4 loading increases to 60 wt %, the E_g^{opt} increases while the T_0 decreases, which may be due to the continuous phase change in the PNCs. In the conjugated polymers, the disorder means the result of variations in conjugation length, rotations, and kinking of polymer chain interactions with neighboring conjugated molecules, impurities, and dipoles from residual solvent molecules.[61] In this work, the disorder is expressed by the resistivity ratio (ρ_r, $\rho_r = \rho_{100}/\rho_{290}$)[62] for the pure PPy and its PNCs. The calculated ρ_r of pure PPy and its PNCs is also listed in Table 2. From Table 2, it is observed that the value of T_0 changes along with the change of ρ_r, indicating that the T_0 depends on the ρ_r (disorder).

3.9. Magnetoresistance. The MR can be calculated using eq 13:[24]

$$MR\% = \frac{R(H) - R(0)}{R(0)} \times 100 \qquad (13)$$

where $R(0)$ is the resistance without magnetic field and $R(H)$ is the resistance under the magnetic field H. In this work, the MR in pure PPy and its Fe_3O_4 PNCs is studied. The room temperature MR values of pure PPy and its Fe_3O_4 PNCs with a Fe_3O_4 nanoparticle loading of 60 wt % are displayed in Figure 10. The MR of the pure PPy shows a positive value within the measured magnetic field range from 0 to 9 T and magnetic field dependent property. This positive MR value for pure PPy is very low and the highest MR value is only about 0.38%. However, the MR of the Fe_3O_4/PPy PNCs with a Fe_3O_4 nanoparticle loading of 60 wt % shows a negative value in the
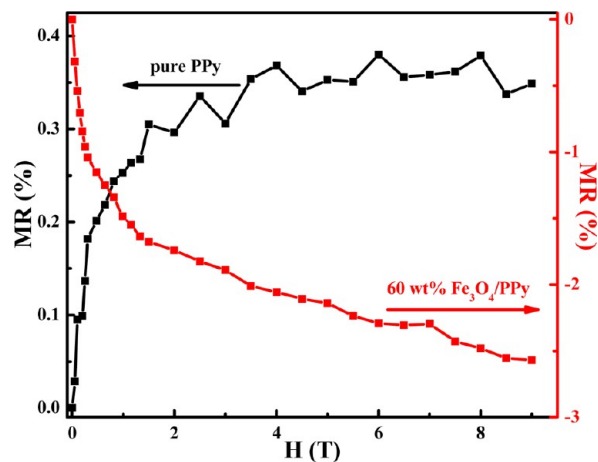

Figure 10. Magnetoresistance of pure PPy and Fe_3O_4/PPy PNCs with a Fe_3O_4 nanoparticle loading of 60 wt %.

measured magnetic field range and decreases with the increasing magnetic field. The negative MR is also observed in the Fe_3O_4/PPy PNCs with Fe_3O_4 nanoparticle loadings of 10, 20, and 40 wt %, respectively.

Generally, the orbital magnetoconductivity theory (forward interference model) and wave function shrinkage model can be used to describe the MR of highly disorderedly localized systems in the VRH regime.[63] In the temperature-dependent resistivity section, the pure PPy and Fe_3O_4/PPy PNCs exhibit the quasi-3-d Mott VRH electrical conduction mechanism. Therefore, these two models can be applied to the pure PPy and 60 wt % Fe_3O_4/PPy PNCs. The wave function shrinkage model is used to describe the positive MR effect of the pure PPy. In the wave function shrinkage model, the $R(H,T)/R(0,T)$ can be expressed as eq 14:[64]

$$R(H, T)/R(0, T) = \exp\{\xi_C(0)[\xi_C(H)/\xi(0) - 1]\} \quad (14)$$

where $\xi_C(0) = (T_0/T)^{1/4}$ for the 3-d Mott VRH charge transport mechanism, $\xi_C(H)/\xi_C(0)$ is the normalized hopping probability parameter and is a function of H/P_C for the Mott VRH charge transport mechanism, H is the magnetic field, and P_C is the fitting parameter, which is the normalizing characteristic field that must be extracted from one set of MR ratio data points and can also be given by eq 15 for the Mott VRH charge transport mechanism:[60,64,65]

$$P_C = 6\hbar/[ea_0^2(T_0/T)^{1/4}] \quad (15)$$

where e is electron charge, and $\hbar$ is the reduced Planck's constant. In the low magnetic field limit, eq 14 is simplified to eq 16:[63]

$$R(H, T)/R(0, T) \approx 1 + t_2 \frac{H^2}{P_C^2}\left(\frac{T_0}{T}\right)^{1/4} \quad (16)$$

And MR is defined as eq 17:

$$
\begin{aligned}
MR &= \frac{R(H, T) - R(0, T)}{R(0, T)} \\
&\approx t_2 \frac{H^2}{P_C^2}\left(\frac{T_0}{T}\right)^{1/4} \\
&= t_2 \frac{e^2 a_0^4}{36\hbar^2}\left(\frac{T_0}{T}\right)^{3/4} H^2
\end{aligned} \quad (17)
$$

where the numerical constant $t_2 = 5/2016$. From eq 17, it is found that the MR value obtained from the wave function shrinkage model will always be positive, hence it is used to explain the positive MR value. According to eq 17, the localization length a_0 can be expressed from the slope of the curve by plotting MR–H^2 ($a_0^4 = ((36\hbar^2 MR)/(t_2 e^2))(T_0/T)^{-(3/4)}H^{-2}$), Figure S2. In Figure S2, the slope of the curve MR–H^2 for the pure PPy is observed to decrease with increasing H^2, which means that the localization length a_0 is reduced with the increasing H. The a_0 can also be calculated from eq 18:

$$a_0^4 = \frac{36\hbar^2 MR}{t_2 e^2}\left(\frac{T_0}{T}\right)^{-3/4} H^{-2} \quad (18)$$

The a_0 is $130.60 \pm 0.97 \times 10^{-6}$, $42.67 \pm 0.03 \times 10^{-6}$, and $28.07 \pm 0.02 \times 10^{-6}$ nm at H of 0.3, 4, and 9 T, respectively. From the obtained results, the a_0 is observed to decrease with increasing H, which is consistent with results in Figure S2.

Thus, the density of states at the Fermi level $N(E_F)$ can be calculated from eq 19 according to eq 11:

$$N(E_F) = 24/[\pi k_B T_0 a_0^3] \quad (19)$$

The obtained $N(E_F)$ is $1.12 \times 10^{34} \pm 1.50 \times 10^{32}$, $1.60 \times 10^{35} \pm 2.16 \times 10^{33}$, and $5.61 \times 10^{35} \pm 7.54 \times 10^{33}$ $(J\ cm^3)^{-1}$ at a_0 of 130.60, 42.67, and 28.07 nm, respectively. The calculated $N(E_F)$ increases with decreasing a_0. Generally, the hopping probability between the localized states increases with increasing $N(E_F)$, indicating that the higher $N(E_F)$, the more hopping probability of charge carriers. The average hopping length R_{hop} can be obtained from eq 20 by T_0, T, and a_0:[66]

$$R_{hop} = (3/8)(T_0/T)^{1/4}a_0 \quad (20)$$

The obtained R_{hop} is $1.72 \times 10^2 \pm 0.58$, $0.56 \times 10^2 \pm 0.19$, and $0.37 \times 10^2 \pm 0.12$ nm at a_0 of 130.60, 42.67, and 28.07 nm, respectively. These results indicate that the R_{hop} decreases with increasing H and the increased MR accompanies with the reduced R_{hop}.

The orbital magnetoconductivity theory is used to investigate the negative MR effect of the Fe_3O_4/PPy PNCs. The effect of interference among various hopping paths was concerned in this theory. These hopping paths include a sequence of scattering of tunneling electrons by the impurities located within a cigar-shaped domain of length r_h (hopping distance) and width $(r_h a_0)^{1/2}$.[63] The ratio $R(H,T)/R(0,T)$ caused by interference effects is described by empirical eq 21:[67]

$$R(H, T)/R(0, T) \approx 1/\{1 + C_{sat}[H/H_{sat}]/[1 + H/H_{sat}]\} \quad (21)$$

where the fitting parameter C_{sat} is constant and also called the temperature-independent fitting parameter and H_{sat} is called the effective saturation magnetic field. As for the Mott VRH electrical conduction mechanism, H_{sat} is calculated by eq 22:[63,68,69]

$$H_{sat} \approx 0.7\left(\frac{8}{3}\right)^{3/2}\left(\frac{1}{a_0^2}\right)\left(\frac{h}{e}\right)\left(\frac{T}{T_0}\right)^{3/8} \quad (22)$$

where h is the Planck's constant, and T_0 is the Mott characteristic temperature (K). In the low-field limit, eq 21 can be simplified to eq 23:

$$R(H, T)/R(0, T) \approx 1 - C_{sat}[H/H_{sat}] \quad (23)$$

Substituting eq 22 into eq 23 and rearranging, the MR can be obtained from eq 24:

$$
\begin{aligned}
MR &= \frac{R(H, T) - R(0, T)}{R(0, T)} \\
&\approx -C_{sat}[H/H_{sat}] \\
&= -C_{sat}\frac{H}{0.7\left(\frac{8}{3}\right)^{3/2}\left(\frac{1}{a_0^2}\right)\left(\frac{h}{e}\right)\left(\frac{T}{T_0}\right)^{3/8}}
\end{aligned} \quad (24)
$$

The calculated a_0 are 0.440, 0.169, and 0.129 μm at H of 0.3, 4, and 8.5 T, respectively. The obtained a_0 for the negative MR value is larger than that of the positive MR value, which is also observed in the carbon nanotube (CNT) films, mat, and pellets at weak magnetic field and interpreted by the quantum interference effect.[70]

10199

dx.doi.org/10.1021/jp402236n | J. Phys. Chem. C 2013, 117, 10191−10202

4. CONCLUSIONS

The conductive PPy PNCs with different Fe_3O_4 nanoparticle loadings have been successfully synthesized by using a facile SIP method. The adding of Fe_3O_4 NPs can enhance the thermal stability of the PPy polymer analyzed by TGA. XRD results indicate that the presence of Fe_3O_4 NPs has significant effects on the crystallization of the PPy. The results from SEM and HRTEM show that the Fe_3O_4 NPs have been embedded in the PPy matrix. The permittivity switching from negative to positive at certain frequency is observed in the fabricated PPy and Fe_3O_4/PPy PNCs. The optical properties of Fe_3O_4/PPy PNCs indicate that the adding of Fe_3O_4 NPs into the PPy has little effect on the E_g^{opt} of PPy. The synthesized Fe_3O_4/PPy PNCs show no hysteresis loop, indicating the superparamagnetic behavior. The resistivity of pure PPy and Fe_3O_4/PPy PNCs decreases with increasing temperature, exhibiting semiconducting behavior. The Mott VRH model is introduced to evaluate the electrical conduction mechanism of these synthesized PPy and its PNCs and the results indicate a quasi-3-d VRH mechanism. The pure PPy shows a positive MR, which is explained based on the wave function shrinkage model, and the Fe_3O_4/PPy PNCs shows a negative MR, which is explained based on the orbital magnetoconductivity theory.

■ ASSOCIATED CONTENT

ⓢ Supporting Information

The dissolution of the Fe_3O_4 NPs and 60 wt % Fe_3O_4/PPy in the 1 mol L^{-1} HCl solution, the MR–H^2 curve, and the calculation method of the localization length a_0 from orbital magnetoconductivity theory. This material is available free of charge via the Internet at http://pubs.acs.org.

■ AUTHOR INFORMATION

Corresponding Author

*E-mail: zhanhu.guo@lamar.edu (Z.G.); suying.wei@lamar.edu (S.W.). Tel.: (409) 880-7654 (Z.G.); (409) 880-7976 (S.W.). Fax: (409) 880-2197 (Z.G.); (409) 880-8270 (S.W.).

Author Contributions

¶These authors are contributed equally in this work.

Notes

The authors declare no competing financial interest.

■ REFERENCES

(1) Zhu, J.; Zhang, X.; Haldolaarachchige, N.; Wang, Q.; Luo, Z.; Ryu, J.; Young, D. P.; Wei, S.; Guo, Z. Polypyrrole Metacomposites with Different Carbon Nanostructures. *J. Mater. Chem.* **2012**, *22*, 4996−5005.

(2) Mavinakuli, P.; Wei, S.; Wang, Q.; Karki, A. B.; Dhage, S.; Wang, Z.; Young, D. P.; Guo, Z. Polypyrrole/Silicon Carbide Nanocomposites with Tunable Electrical Conductivity. *J. Phys. Chem. C* **2010**, *114*, 3874−3882.

(3) Zhu, J.; Wei, S.; Zhang, L.; Mao, Y.; Ryu, J.; Haldolaarachchige, N.; Young, D. P.; Guo, Z. Electrical and Dielectric Properties of Polyaniline−Al₂O₃ Nanocomposites Derived from Various Al₂O₃ Nanostructures. *J. Mater. Chem.* **2011**, *21*, 3952−3959.

(4) Wei, H.; Yan, X.; Li, Y.; Wu, S.; Wang, A.; Wei, S.; Guo, Z. Hybrid Electrochromic Fluorescent Poly(DNTD)/CdSe@ZnS Composite Films. *J. Phys. Chem. C* **2012**, *116*, 4500−4510.

(5) Zhang, D.; Zhang, X.; Chen, Y.; Yu, P.; Wang, C.; Ma, Y. Enhanced Capacitance and Rate Capability of Graphene/Polypyrrole Composite as Electrode Material for Supercapacitors. *J. Power Sources* **2011**, *196*, 5990−5996.

(6) Wei, S.; Mavinakuli, P.; Wang, Q.; Chen, D.; Asapu, R.; Mao, Y.; Haldolaarachchige, N.; Young, D. P.; Guo, Z. Polypyrrole-titania Nanocomposites Derived from Different Oxidants. *J. Electrochem. Soc.* **2011**, *158*, K205−K212.

(7) Guo, Z.; Shin, K.; Karki, A. B.; Young, D. P.; Kaner, R. B.; Hahn, H. T. Fabrication and Characterization of Iron Oxide Nanoparticles Filled Polypyrrole Nanocomposites. *J. Nanopart. Res.* **2009**, *11*, 1441−1452.

(8) Gu, H.; Huang, Y.; Zhang, X.; Wang, Q.; Zhu, J.; Shao, L.; Haldolaarachchige, N.; Young, D. P.; Wei, S.; Guo, Z. Magnetoresistive Polyaniline-magnetite Nanocomposites with Negative Dielectrical Properties. *Polymer* **2012**, *53*, 801−809.

(9) Duffy, J. A.; Taylor, J. W.; Dugdale, S. B.; Shenton Taylor, C.; Butchers, M. W.; Giblin, S. R.; Cooper, M. J.; Sakurai, Y.; Itou, M. Spin and Orbital Moments in Fe₃O₄. *Phys. Rev. B* **2010**, *81*, 134424.

(10) Coey, J.; Chien, C. Half-metallic Ferromagnetic Oxides. *MRS Bull.* **2003**, *28*, 720−724.

(11) Niranjan, M. K.; Velev, J. P.; Duan, C.-G.; Jaswal, S. S.; Tsymbal, E. Y. Magnetoelectric Effect at the Fe₃O₄/BaTiO₃(001) Interface: A First-Principles Study. *Phys. Rev. B* **2008**, *78*, 104405.

(12) Gu, H.; Rapole, S.; Sharma, J.; Huang, Y.; Cao, D.; Colorado, H. A.; Luo, Z.; Haldolaarachchige, N.; Young, D. P.; Wei, S.; et al. Magnetic Polyaniline Nanocomposites toward Toxic Hexavalent Chromium Removal. *RSC Adv.* **2012**, *2*, 11007−11018.

(13) Gu, H.; Tadakamalla, S.; Huang, Y.; Colorado, H. A.; Luo, Z.; Haldolaarachchige, N.; Young, D. P.; Wei, S.; Guo, Z. Polyaniline Stabilized Magnetite Nanoparticle Reinforced Epoxy Nanocomposites. *ACS Appl. Mater. Interfaces* **2012**, *4*, 5613−5624.

(14) Wei, S.; Wang, Q.; Zhu, J.; Sun, L.; Guo, Z. Multifunctional Composite Core−Shell Nanoparticles. *Nanoscale* **2011**, *3*, 4474−4502.

(15) Dey, A.; De, A.; De, S. K. Electrical Transport and Dielectric Relaxation in Fe₃O₄-polypyrrole Hybrid Nanocomposites. *J. Phys.: Condens. Matter* **2005**, *17*, 5895−5910.

(16) Chen, A.; Wang, H.; Zhao, B.; Li, X. The Preparation of Polypyrrole−Fe₃O₄ Nanocomposites by the Use of Common Ion Effect. *Synth. Met.* **2003**, *139*, 411−415.

(17) Wuang, S. C.; Neoh, K. G.; Kang, E.-T.; Pack, D. W.; Leckband, D. E. Synthesis and Functionalization of Polypyrrole-Fe₃O₄ Nanoparticles for Applications in Biomedicine. *J. Mater. Chem.* **2007**, *17*, 3354−3362.

(18) Chen, W.; Li, X.; Xue, G.; Wang, Z.; Zou, W. Magnetic and Conducting Particles: Preparation of Polypyrrole Layer on Fe₃O₄ Nanospheres. *Appl. Surf. Sci.* **2003**, *218*, 216−222.

(19) Li, X.; Wan, M.; Wei, Y.; Shen, J.; Chen, Z. Electromagnetic Functionalized and Core-shell Micro/Nanostructured Polypyrrole Composites. *J. Phys. Chem. B* **2006**, *110*, 14623−14626.

(20) Smith, D.; Pendry, J.; Wiltshire, M. Metamaterials and Negative Refractive Index. *Science* **2004**, *305*, 788−792.

(21) Nalwa, H. S. *Handbook of Organic Conductive Molecules and Polymers: Conductive Polymers: Spectroscopy and Physical Properties*; Wiley: New York, NY, 1997; p 368.

(22) Leonhardt, U. Optical Metamaterials: Invisibility Cup. *Nat. Photonics* **2007**, *1*, 207−208.

(23) Zhu, J.; Gu, H.; Luo, Z.; Haldolaarachige, N.; Young, D. P.; Wei, S.; Guo, Z. Carbon Nanostructure-derived Polyaniline Metacomposites: Electrical, Dielectric, and Giant Magnetoresistive Properties. *Langmuir* **2012**, *28*, 10246−10255.

(24) Hu, B.; Wu, Y. Tuning Magnetoresistance Between Positive and Negative Values in Organic Semiconductors. *Nat. Mater.* **2007**, *6*, 985−991.

10200

dx.doi.org/10.1021/jp402236n | *J. Phys. Chem. C* 2013, 117, 10191−10202

(25) Bloom, F.; Kemerink, M.; Wagemans, W.; Koopmans, B. Sign Inversion of Magnetoresistance in Space-charge Limited Organic Devices. *Phys. Rev. Lett.* 2009, *103*, 66601.

(26) Desai, P.; Shakya, P.; Kreouzis, T.; Gillin, W.; Morley, N.; Gibbs, M. Magnetoresistance and Efficiency Measurements of Alq_3-based OLEDs. *Phys. Rev. B* 2007, *75*, 094423.

(27) Abou-Elazab, T.; Migahed, M.; Park, H.; Park, Y.; MacNeillis, P.; Rabenau, T.; Roth, S. Magnetoresistance of Polypyrrole and Polyacetylene. *Synth. Met.* 1996, *76*, 281−284.

(28) Long, Y.; Chen, Z.; Zhang, X.; Zhang, J.; Liu, Z. Electrical Properties of Multi-walled Carbon Nanotube/Polypyrrole Nanocables: Percolation-dominated Conductivity. *J. Phys. D: Appl. Phys.* 2004, *37*, 1965−1969.

(29) Deng, J.; He, C.; Peng, Y.; Wang, J.; Long, X.; Li, P.; Chan, A. S. C. Magnetic and Conductive Fe_3O_4−Polyaniline Nanoparticles with Core−Shell Structure. *Synth. Met.* 2003, *139*, 295−301.

(30) Wang, L.; Yu, Y.; Chen, P.; Zhang, D.; Chen, C. Electrospinning Synthesis of C/Fe_3O_4 Composite Nanofibers and Their Application for High Performance Lithium-Ion Batteries. *J. Power Sources* 2008, *183*, 717−723.

(31) Zhang, H.; Zhong, X.; Xu, J.-J.; Chen, H.-Y. Fe_3O_4/Polypyrrole/ Au Nanocomposites with Core/Shell/Shell Structure: Synthesis, Characterization, and Their Electrochemical Properties. *Langmuir* 2008, *24*, 13748−13752.

(32) Zhu, J.; Wei, S.; Zhang, L.; Mao, Y.; Ryu, J.; Mavinakuli, P.; Karki, A. B.; Young, D. P.; Guo, Z. Conductive Polypyrrole/Tungsten Oxide Metacomposites with Negative Permittivity. *J. Phys. Chem. C* 2010, *114*, 16335−16342.

(33) Tung, N. T.; Lee, H.; Song, Y.; Nghia, N. D.; Sohn, D. Structure and Properties of Selenious Acid Doped Polyaniline with Varied Dopant Content. *Synth. Met.* 2010, *160*, 1303−1306.

(34) Zhang, X.; Zhu, J.; Haldolaarachchige, N.; Ryu, J.; Young, D. P.; Wei, S.; Guo, Z. Synthetic Process Engineered Polyaniline Nanostructures with Tunable Morphology and Physical Properties. *Polymer* 2012, *53*, 2109−2120.

(35) Schonhals, A.; Kremer, R. Analysis of Dielectric Spectra. *Broadband Dielectric Spectroscopy*; Springer: New York, NY,2003; p 59.

(36) Rosenbaum, R.; Milner, A.; Haberkern, R.; Häussler, P.; Palm, E.; Murphy, T.; Hannahs, S.; Brandt, B. Magnetoresistance of an Insulating Quasicrystalline AlPdRe Film in Large Magnetic Fields. *J. Phys.: Condens. Matter* 2001, *13*, 3169−3185.

(37) Hsieh, C.-H.; Lee, A.-H.; Liu, C.-D.; Han, J.-L.; Hsieh, K.-H.; Lee, S.-N. Polyaniline Nano-composites with Large Negative Dielectric Permittivity. *AIP Adv.* 2012, *2*, 012127.

(38) Yao, J.; Liu, Z.; Liu, Y.; Wang, Y.; Sun, C.; Bartal, G.; Stacy, A. M.; Zhang, X. Optical Negative Refraction in Bulk Metamaterials of Nanowires. *Science* 2008, *321*, 930.

(39) Gu, H.; Tadakamalla, S.; Zhang, X.; Huang, Y.-D.; Jiang, Y.; Colorado, H. A.; Luo, Z.; Wei, S.; Guo, Z. Epoxy Resin Nanosuspensions and Reinforced Nanocomposites from Polyaniline Stabilized Multi-Walled Carbon Nanotubes. *J. Mater. Chem. C* 2012, *1*, 729−743.

(40) Chen, H.; Ran, L.; Huangfu, J.; Zhang, X.; Chen, K.; Grzegorczyk, T. M.; Kong, J. A. Metamaterial Exhibiting Left-handed Properties over Multiple Frequency Bands. *J. Appl. Phys.* 2004, *96*, 5338−5340.

(41) Magnus, F.; Wood, B.; Moore, J.; Morrison, K.; Perkins, G.; Fyson, J.; Wiltshire, M.; Caplin, D.; Cohen, L.; Pendry, J. A d.c. Magnetic Metamaterial. *Nat. Mater.* 2008, *7*, 295−297.

(42) Liang, Z.; Gregg, B. A. Compensating Poly(3-hexylthiophene) Reveals Its Doping Density and Its Strong Exciton Quenching by Free Carriers. *Adv. Mater.* 2012, *24*, 3258−3262.

(43) Hill, I. G.; Kahn, A.; Soos, Z. G.; Pascal, J. R. A. Charge-separation Energy in Films of π-conjugated Organic Molecules. *Chem. Phys. Lett.* 2000, *327*, 181−188.

(44) Yu, J.; Xiang, Q.; Zhou, M. Preparation, Characterization and Visible-light-driven Photocatalytic Activity of Fe-doped Titania Nanorods and First-principles Study for Electronic Structures. *Appl. Catal., B* 2009, *90*, 595−602.

(45) Farag, A.; Ashery, A.; Rafea, M. A. Optical Dispersion and Electronic Transition Characterizations of Spin Coated Polyaniline Thin Films. *Synth. Met.* 2010, *160*, 156−161.

(46) Bora, C.; Dolui, S. Fabrication of Polypyrrole/Graphene Oxide Nanocomposites by Liquid/Liquid Interfacial Polymerization and Evaluation of Their Optical, Electrical and Electrochemical Properties. *Polymer* 2012, *53*, 923−932.

(47) Jang, J.; Oh, J. H. Fabrication of a Highly Transparent Conductive Thin Film from Polypyrrole/Poly(methyl methacrylate) Core/Shell Nanospheres. *Adv. Funct. Mater.* 2005, *15*, 494−502.

(48) Håkansson, E.; Lin, T.; Wang, H.; Kaynak, A. The Effects of Dye Dopants on the Conductivity and Optical Absorption Properties of Polypyrrole. *Synth. Met.* 2006, *156*, 1194−1202.

(49) Veselago, V. G. The Electrodynamics of Substances with Simultaneously Negative Values of ε and μ. *Phys.-Usp.* 1968, *10*, 509−514.

(50) Guo, Z.; Hahn, H. T.; Lin, H.; Karki, A. B.; Young, D. P. Magnetic and Magnetoresistance Behaviors of Particulate Iron/Vinyl Ester Resin Nanocomposites. *J. Appl. Phys.* 2008, *104*, 014314.

(51) Capolino, F. *Theory and Phenomena of Metamaterials*; CRC Press: Boca Raton, FL, 2009.

(52) Wei, H.; Zhu, J.; Wu, S.; Wei, S.; Guo, Z. Electrochromic Polyaniline/Graphite Oxide Nanocomposites with Endured Electrochemical Energy Storage. *Polymer* 2013, *54*, 1820−1831.

(53) Gonçalves, G.; Baldissera, A.; Rodrigues, L.; Martini, E.; Ferreira, C. Alkyd Coatings Containing Polyanilines for Corrosion Protection of Mild Steel. *Synth. Met.* 2011, *161*, 313−323.

(54) Zhang, D.; Karki, A. B.; Rutman, D.; Young, D. P.; Wang, A.; Cocke, D.; Ho, T. H.; Guo, Z. Electrospun Polyacrylonitrile Nanocomposite Fibers Reinforced with Fe_3O_4 Nanoparticles: Fabrication and Property Analysis. *Polymer* 2009, *50*, 4189−4198.

(55) Dhawan, S. K.; Singh, N.; Rodrigues, D. Electromagnetic Shielding Behaviour of Conducting Polyaniline Composites. *Sci. Technol. Adv. Mater.* 2003, *4*, 105−113.

(56) Guo, Z.; Zhang, D.; Wei, S.; Wang, Z.; Karki, A.; Li, Y.; Bernazzani, P.; Young, D.; Gomes, J.; Cocke, D.; Ho, T. Effects of Iron Oxide Nanoparticles on Polyvinyl Alcohol: Interfacial Layer and Bulk Nanocomposites Thin Film. *J. Nanopart. Res.* 2010, *12*, 2415−2426.

(57) Zhang, L.; Tang, Z.-J. Polaron Relaxation and Variable-range-hopping Conductivity in The Giant-dielectric-constant Material $CaCu_3Ti_4O_{12}$. *Phys. Rev. B* 2004, *70*, 174306.

(58) Zhu, J.; Wei, S.; Zhang, L.; Mao, Y.; Ryu, J.; Karki, A. B.; Young, D. P.; Guo, Z. Polyaniline-tungsten Oxide Metacomposites with Tunable Electronic Properties. *J. Mater. Chem.* 2011, *21*, 342−348.

(59) Zhu, J.; Wei, S.; Zhang, L.; Mao, Y.; Ryu, J.; Haldolaarachige, N.; Young, D. P.; Guo, Z. Electrical and Dielectric Properties of Polyaniline-Al_2O_3 Nanocomposites Derived from Various Al_2O_3 Nanostructures. *J. Mater. Chem.* 2011, *21*, 3952−3959.

(60) Bhadra, S.; Khastgir, D.; Singha, N. K.; Lee, J. H. Progress in Preparation, Processing and Applications of Polyaniline. *Prog. Polym. Sci.* 2009, *34*, 783−810.

(61) Blakesley, J. C.; Neher, D. Relationship between Energetic Disorder and Open-circuit Voltage in Bulk Heterojunction Organic Solar Cells. *Phys. Rev. B* 2011, *84*, 075210.

(62) Sarkar, A.; Ghosh, P.; Meikap, A.; Chattopadhyay, S.; Chatterjee, S.; Ghosh, M. Direct and Alternate Current Conductivity and Magnetoconductivity of Oxalic Acid Doped Polyaniline. *Solid State Commun.* 2007, *143*, 358−363.

(63) Su, T.-I.; Wang, C.-R.; Lin, S.-T.; Rosenbaum, R. Magnetoresistance of $Al_{70}Pd_{22.5}Re_{7.5}$ Quasicrystals in the Variable-range Hopping Regime. *Phys. Rev. B* 2002, *66*, 054438.

(64) Rosenbaum, R.; Murphy, T.; Palm, E.; Hannahs, S.; Brandt, B. Magnetoresistance of Insulating Amorphous Ni_xSi_{1-x} Films Exhibiting Mott Variable-range Hopping Laws. *Phys. Rev. B* 2001, *63*, 094426.

(65) Gu, H.; Guo, J.; Zhang, X.; He, Q.; Huang, Y.; Colorado, H. A.; Haldolaarachchige, N.; Xin, H.; Young, D. P.; Wei, S.; Guo, Z. Giant Magnetoresistive Phosphoric Acid Doped Polyaniline−silica Nanocomposites. *J. Phys. Chem. C* 2013, *117*, 6426−6436.

(66) Shalaev, V. M. Optical Negative-index Metamaterials. *Nat. Photonics* **2007**, *1*, 41−48.

(67) Hoffman, A. J.; Alekseyev, L.; Howard, S. S.; Franz, K. J.; Wasserman, D.; Podolskiy, V. A.; Narimanov, E. E.; Sivco, D. L.; Gmachl, C. Negative Refraction in Semiconductor Metamaterials. *Nat. Mater.* **2007**, *6*, 946−950.

(68) Sarkar, A.; Ghosh, P.; Meikap, A. K.; Chattopadhyay, S. K.; Chatterjee, S. K.; Ghosh, M. Direct and Alternate Current Conductivity and Magnetoconductivity of Oxalic Acid Doped Polyaniline. *Solid State Commun.* **2007**, *143*, 358−363.

(69) Gu, H.; Zhang, X.; Wei, H.; Wei, S.; Guo, Z. Magnetoresistance Phenomenon Overview in Molecular Systems. *Chem. Soc. Rev.* **2013**, DOI: 10.1039/C3CS60074B.

(70) Long, Y.; Chen, Z.; Zhang, X.; Zhang, J.; Liu, Z. Synthesis and Electrical Properties of Carbon Nanotube Polyaniline Composites. *Appl. Phys. Lett.* **2004**, *85*, 1796−1798.

■ NOTE ADDED AFTER ASAP PUBLICATION

This paper was published on the Web on May 6, 2013. A revision was made in the Results and Discussion section. The revised version was reposted May 8, 2013.

10202

dx.doi.org/10.1021/jp402236n | *J. Phys. Chem. C* 2013, 117, 10191−10202